BIOCHEMISTRY
including biophysical chemistry & molecular biology

Article

pubs.acs.org/biochemistry

Man o' War Mutation in UDP-α-D-Xylose Synthase Favors the Abortive Catalytic Cycle and Uncovers a Latent Potential for Hexamer Formation

Richard M. Walsh, Jr.,[†] Samuel J. Polizzi,[‡] Renuka Kadirvelraj, Wesley W. Howard,[§] and Zachary A. Wood*

Department of Biochemistry and Molecular Biology, University of Georgia, Athens, Georgia 30602, United States

Supporting Information

ABSTRACT: The *man o' war* (*mow*) phenotype in zebrafish is characterized by severe craniofacial defects due to a missense mutation in UDP-α-D-xylose synthase (UXS), an essential enzyme in proteoglycan biosynthesis. The *mow* mutation is located in the UXS dimer interface ~16 Å away from the active site, suggesting an indirect effect on the enzyme mechanism. We have examined the structural and catalytic consequences of the *mow* mutation (R236H) in the soluble fragment of human UXS (hUXS), which shares 93% sequence identity with the zebrafish enzyme. In solution, hUXS dimers undergo a concentration-dependent association to form a tetramer. Sedimentation velocity studies show that the R236H substitution induces the formation of a new hexameric species. Using two new crystal structures of the hexamer, we show that R236H and R236A substitutions cause a local unfolding of the active site that allows for a rotation of the dimer interface necessary to form the hexamer. The disordered active sites in the R236H and R236A mutant constructs displace Y231, the essential acid/base catalyst in the UXS reaction mechanism. The loss of Y231 favors an abortive catalytic cycle in which the reaction intermediate, UDP−α-D-4-keto-xylose, is not reduced to the final product, UDP−α-D-xylose. Surprisingly, the *mow*-induced hexamer is almost identical to the hexamers formed by the deeply divergent UXS homologues from *Staphylococcus aureus* and *Helicobacter pylori* (21% and 16% sequence identity, respectively). The persistence of a latent hexamer-building interface in the human enzyme suggests that the ancestral UXS may have been a hexamer.

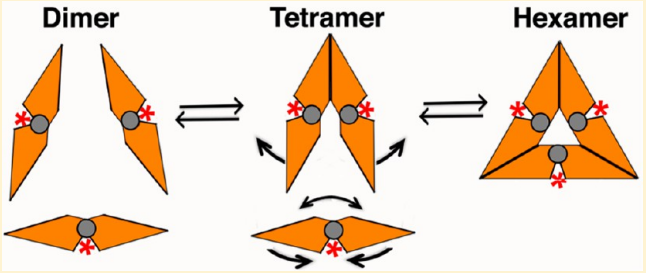

Proteoglycans provide structural integrity to connective tissues such as the extracellular matrix, cartilage, and bone.[1−3] Most proteoglycans consist of a glycosaminoglycan (GAG) connected to a protein core by a conserved tetrasaccharide linker (Figure 1A). The biosynthesis of the tetrasaccharide linker begins with the covalent attachment of xylose to a serine hydroxyl, followed by two galactose residues and a glucuronic acid molecule.[1,4,5] The *man o' war* (*mow*) mutation in zebrafish disrupts proteoglycan biosynthesis, resulting in severe craniofacial defects.[6] This mutation has been mapped to a single missense substitution in the gene for UDP-α-xylose synthase (UXS), the enzyme that produces the UDP-sugar donor for the essential xylose in proteoglycan biosynthesis.[6] Zebrafish and human UXS (hUXS) share an overall sequence identity of 89% with much of the variation occurring in the 84-residue N-terminal transmembrane domain (in the absence of the trans-membrane domain, the sequence identity is 93%). We have previously shown that the *mow* mutation (R236H) in hUXS (hUXS^{mow}) prevents the synthesis of UDP-α-D-xylose (UDP-Xyl).[6] The disruption of proteoglycan biosynthesis has been shown to attenuate tumor growth and progression.[2,3,7,8] Thus, understanding the molecular basis by which the *mow* mutation inactivates hUXS may facilitate the development of new strategies to control proteoglycan synthesis.

In hUXS, the N-terminal transmembrane helix anchors the enzyme to the luminal face of the endoplasmic reticulum.[9−11] The recombinant enzyme lacking the transmembrane helix purifies with stoichiometric amounts of tightly bound NAD^+ cofactor that is recycled through successive oxidation and reduction steps in the catalytic mechanism (Figure 1B).[12] In the first step, NAD^+ oxidizes UDP-α-D-glucuronic acid (UDP-GlcA) to produce NADH and UDP-α-D-4-keto-xylose (UDP-4-keto-Xyl). Next, NADH reduces the ketose intermediate to produce UDP-Xyl. During turnover the NADH and UDP-4-keto-Xyl intermediates can be released in an abortive cycle that generates the inactive apoenzyme (Figure 1B).[12] The inactive enzyme can be rescued by adding exogenous NAD^+ to the reaction.[12] Because of the bifurcated mechanism, hUXS in the presence of saturating NAD^+ will produce both UDP-Xyl and the reaction intermediates NADH and UDP-4-keto-Xyl.

Received: October 31, 2014
Revised: December 12, 2014
Published: December 18, 2014

DOI: 10.1021/bi501357c
Biochemistry 2015, 54, 807−819

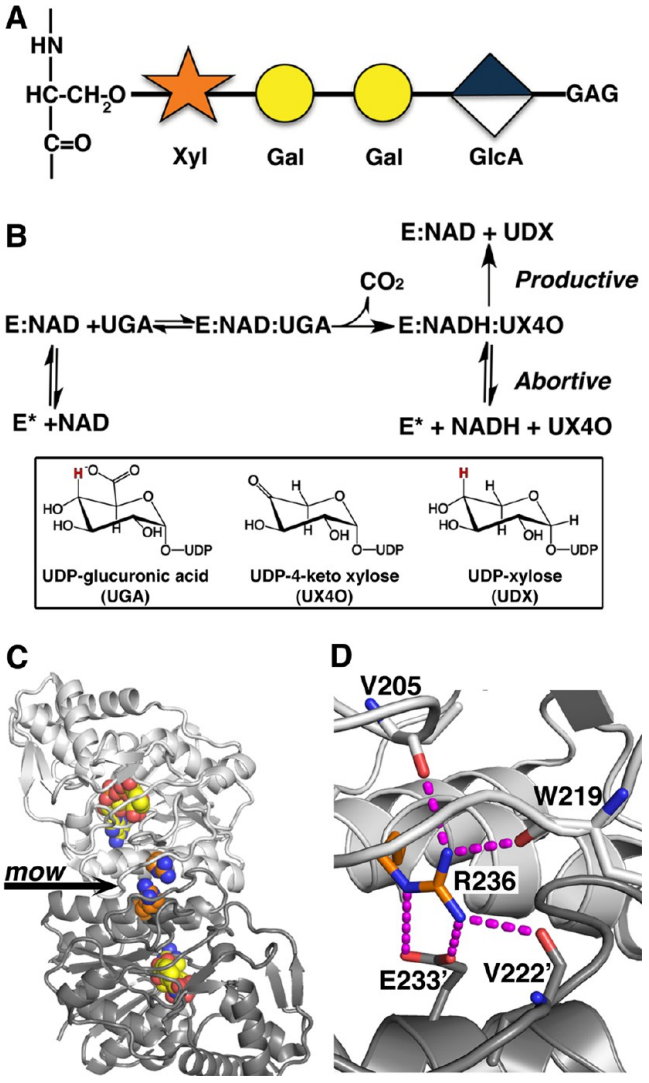

Figure 1. hUXS produces UDP-xylose for proteoglycan biosynthesis. (A) hUXS produces UDP-Xyl, the sugar donor for the first residue in the conserved tetrasaccharide linker that tethers GAG to proteins. (B) The hUXS reaction begins with the oxidative decarboxylation of UDP-glucuronic acid (UGA) to form the intermediate ternary complex containing NADH and UDP-4-keto-xylose (E:NADH:UX4O). Here the mechanism is split into the productive and abortive pathways.[12] In the productive pathway (top) the UX4O is reduced to UDP-Xyl (UDX) and the NAD^+ cofactor is regenerated. In the abortive pathway (bottom) the E:NADH:UX4O complex releases the intermediates and the apoenzyme, E*, can be rescued by exogenous NAD^+. The nucleotide sugars are identified in the box below the pathway. (C) The *mow* mutation (arrow) is located in the interface of the hUXS dimer (light and dark gray cartoons). R236 is depicted as orange spheres with atomic coloring. The NAD^+ cofactor (yellow with atomic coloring) illustrates the relationship to the mutation sites. (D) The electrostatic interactions (magenta dashed lines) of R236 in the wild-type hUXS structure (PDB code 2B69). The electrostatic interaction between R236 and E233 is not necessarily a hydrogen bond based on the less than ideal geometry (N–H···O angles ≈ 145°).

hUXS is a member of the "extended" short-chain dehydrogenase/reductase family (SDR) of enzymes, which typically form dimers or tetramers.[13,14] Recently, we have shown that hUXS undergoes a concentration-dependent association in solution to produce a mixture of monomers, dimers, and tetramers.[15] The formation of the hUXS tetramer increases the rate of UDP-Xyl production 6-fold while the abortive release of the reaction intermediates increases by only 20%.[15] The preferential increase in UDP-Xyl production suggests that the tetramer is the catalytically important species (Figure 1B). The *mow* mutation (R236H) is buried in the dimer interface of hUXS, located approximately 16 Å away from the active site (Figure 1C,D). Earlier work suggested that the R236H mutation might inactivate the enzyme by disrupting the dimeric structure.[6] Here we show that the loss of activity in $hUXS^{mow}$ is due to a local unfolding of the active site that disorders a key catalytic tyrosine. We also combine solution studies with two new crystal structures of $hUXS^{mow}$ to show that the *mow* mutation induces the formation of a hexameric complex that is almost identical to that observed in deeply divergent homologues.

MATERIALS AND METHODS

Protein Expression, Crystallization, Data Collection, and Structure Solution. All residues numbers herein refer to full-length hUXS. To produce soluble protein, $hUXS_{R236H}$, $hUXS_{R236A}$, and $hUXS_{Y231F}$ constructs lacking the 84-residue N-terminal transmembrane domain were generated by Norclone Biotech Laboratories (London, Canada). The protein was expressed and purified as previously described.[6] $hUXS_{R236H}$ and $hUXS_{R236A}$ were dialyzed into 20 mM Tris (pH 8.0) with 250 mM NaCl and concentrated to 10 mg/mL for crystallization. $hUXS_{R236H}$ containing 5 mM UDP and UXS_{R236A} containing 10 mM UDP-GlcA were screened for crystallization at 25 and 20 °C, respectively. Crystals were grown using the hanging drop vapor diffusion method with 2 μL drops mixed in a 1:1 protein-to-reservoir ratio. The reservoir contained 0.5 M ammonium sulfate, 0.5 M sodium acetate, 0.1 M imidazole, and 0.1 M HCl at pH 5.95 for $hUXS_{R236H}$ and 0.1 M ammonium sulfate, 0.1 M succinate at pH 5.4, and 10% DMSO for $hUXS_{R236A}$, respectively. Crystals grew as hexagonal rods within 21 days and were cryoprotected by passing through either 50:50 paratone/paraffin oil ($hUXS_{R236H}$) or reservoir solution containing 15% DMSO ($hUXS_{R236A}$) and then cooled by plunging directly into liquid nitrogen. Data sets at 2.86 Å ($hUXS_{R236H}$) and 2.64 Å ($hUXS_{R236A}$) resolution were collected at the 22-ID beamline (SER-CAT) at the Argonne National Laboratory (Illinois) using a MAR 300 mm ($hUXS_{R236H}$) or 225 mm ($hUXS_{R236A}$) CCD detector, a wavelength of 1 Å, and an oscillation step size of 1°. The data were processed with XDS[16] and 5% of the data were set aside for cross-validation (Table 1).[17] In the 3.1–3.0 Å resolution bin of the $hUXS_{R236H}$ data, the $\langle I/\sigma \rangle$ is 2.1 but the R_{meas} is 116.1. R_{merge}-based statistics describe the spread of data (precision) but not data accuracy. To estimate the accuracy of the data, we used the $CC_{1/2}$ indicator developed by Karplus and Diedrichs.[18] $CC_{1/2}$ values to 0.5 have been shown to accurately predict usable data below $\langle I/\sigma \rangle$ of 2.0 and with $R_{meas} > 300$. The $CC_{1/2}$ value shows that we have usable data to 2.86 Å resolution for Table 1. Thus, we used all data to 2.86 Å resolution in refinement of $hUXS_{R236H}$, but we also report statistics to 3.0 Å resolution for comparison to structures refined with previous standards.

The crystal structures of R236H and R236A were solved by molecular replacement using the structure of wild-type hUXS monomer (PDB entry 2B69) lacking cofactors and ligands as a search model in the program Phaser.[19] The molecular replacement solutions were then subjected to rigid-body refinement using PHENIX[20] followed by iterative cycles of manual building and positional refinement using Coot and

DOI: 10.1021/bi501357c
Biochemistry 2015, 54, 807–819

Table 1. Data Collection and Refinement Statistics

	$hUXS_{R236H}$	$hUXS_{R236A}$
Data Collection		
Protein Data Bank entry	4M55	4LK3
space group	$P2_12_12_1$	$P2_12_12_1$
unit cell dimensions *a*, *b*, *c* (Å)	83.2, 85.2, 292.6	83.6, 92.1, 291.0
completeness (%)	99.3 (92.8)[a] [99.1][b]	98.4 (89.6)[a]
unit cell redundancy	6.1 (5.9) [5.96]	11.9 (10.4)
no. of reflections	261 957	781 865
I/σ (I)	13.1 (2.1) [1.2]	20.5 (2.9)
$CC_{1/2}$[c]	0.998 (0.76) [0.50]	0.999 (0.82)
R_{meas}[d] (%)	12.3 (116.1) [200.7]	9.7 (85.9)
$R_{mrgd\text{-}F}$[e] (%)	11.2 (105.8) [183.0]	9.3 (81.7)
R_{pim}[f] (%)	4.9 (47.9) [81.4]	2.8 (25.9)
Refinement		
resolution (Å)	2.86 (3.1−3.0) [2.96−2.86]	2.64 (2.73−2.64)
R_{work}/R_{free}	0.218/0.279[g]	0.198/0.245
R_{free} in highest resolution shell	(0.376) [0.461]	(0.384)
no. atoms protein/ligand/water	11 146/337/0	12 724/633/74
B-factors protein/ligand/water ($Å^2$)	116.7/110.8/n.a.	80.3/79.9/60.7
Stereochemical Ideality		
bond lengths (Å)	0.018	0.019
bond angles (deg)	1.40	1.75
φ,ψ preferred region (%)	95.9	97.4
φ,ψ additionally allowed (%)	4.1	2.6
φ,ψ disallowed region (%)	0.0	0.0

[a]Values in parentheses are for the highest-resolution shell (3.1−3.0) based on an I/σ cutoff of 2. [b]Values in brackets are for the highest-resolution shell [2.96−2.86] used in refinement of R236H based on the $CC_{1/2}$ cutoff defined by Diederichs and Karplus.[18] For R236A, due to a less than optimal detector distance, the highest resolution shell of data collected had an I/σ of 2.9 so we did not incorporate the $CC_{1/2}$ cutoff. [c]$CC_{1/2}$ is the percentage of correlation between intensities from random half-data sets.[18] [d]R_{meas} is the redundancy independent merging *R*-factor.[39] [e]$R_{mrgd\text{-}F}$ is the measure of reduced data accuracy.[39] [f]R_{pim} is the merging *R*-factor that indicates precision.[40,41] [g]Refers to data to 3.0 Å. The R_{work}/R_{free} to 2.86 Å is 0.228/0.285.

PHENIX, respectively.[20,21] Crystal parameters, data collection and refinement statistics are reported in Table 1. Domain rotations were identified using DynDom.[22] Interface solvent accessible area calculations were carried out using the *Protein interfaces, surfaces and assemblies* service (PISA) at the European Bioinformatics Institute.[23] Structure-based sequence alignments were carried out using Sequoia.[24]

Sedimentation Velocity Analytical Ultracentrifugation. For sedimentation velocity analysis, $hUXS_{R236H}$ was dialyzed into phosphate-buffered saline at pH 7.5 using a microdialyzer system (Pierce) and loaded into 12 mm cells with double-sector Epon centerpieces equipped with quartz windows and equilibrated for 1 h at 20 °C in an An60 Ti rotor. Sedimentation velocity data were collected in an Optima XLA analytical ultracentrifuge using a rotor speed of 50 000 rpm at 20 °C. Data were recorded at wavelengths of 230 nm (0.5 μM $hUXS_{R236H}$) or 280 nm (21 μM $hUXS_{R236H}$) using a radial step size of 0.003 cm. A partial specific volume of 0.735 mL/g was calculated from the amino acid sequence of N-terminal-truncated hUXS. The buffer viscosity of 1.019 cP and density of 1.006 g/mL were calculated using the program SEDNTERP.[25] Data were analyzed using the program SEDFIT. Continuous sedimentation coefficient distribution ($c(s)$) analyses were restrained by maximum entropy regularization at $P = 0.68$ confidence interval and the baseline, meniscus, frictional coefficient, systematic time-invariant, and radial-invariant noise were fit.[26] Theoretical sedimentation coefficient (s) values for the monomer and dimer were calculated using the hUXS atomic coordinates (4GLL) under standard conditions with the program HYDROPRO.[27] For the *mow* constructs, the hUXS structure (PDB code 2B69) was superimposed onto the $hUXS^{mow}$ coordinates to generate the *s* values.

Enzyme Activity. The release of the reaction intermediate, NADH, from hUXS variants was recorded as an increase in absorbance at 340 nm using an Agilent 8453 UV−vis spectrophotometer equipped with a Peltier temperature controller set to 25 °C, as previously described.[12] The experiments were performed under standard conditions with 1 mg/mL enzyme in a reaction buffer containing 50 mM Tris at pH 8.0, 25 mM NaCl, and 1 mM EDTA. The enzyme and substrate (5 mM each UDP-GlcA and NAD^+) solutions were preincubated separately at 25 °C. The reaction was initiated by a rapid manual mixing of the two solutions and the release rates were determined in triplicate. The reaction products of hUXS and the R236 substitution constructs were determined using a G1600 3D capillary electrophoresis system (Agilent Technologies) as previously described.[12] Product assays were conducted using assay conditions with 5 mM UDP-GlcA and 2.5 mM NAD^+. Reactions were allowed to proceed for 1 h and were then quenched and extracted with 1:1 v/v chloroform. Capillary zone electrophoresis (CZE) of the aqueous layer was performed in a fused-silica capillary (56 cm × 50 μm) with an extended light path using 20 mM borate at pH 9.3 as the background electrolyte at 22 kV and a temperature of 18 °C. Absorbance spectra were collected between wavelengths of 200 and 400 nm, and the enzyme reaction products were identified by comigration with known standards.

RESULTS

Solution Structure of $hUXS_{R236H}$ Reveals a Hexamer. To determine the effect of the *mow* mutation on the oligomeric state of hUXS, we analyzed the structures of hUXS and $hUXS_{R236H}$ using sedimentation velocity (Figure 2). At low protein concentrations (0.5 μM) hUXS sediments as a single broad peak at 4.6 S, close to the predicted value for the hUXS dimer (5.0 S) (Figure 2A). The widths of the peak and the tailing at both low and high *s* values were previously shown to indicate the presence of a small amount of monomer and tetramer in rapid equilibrium with the dimer (Figure 2A).[15] At the same concentration of protein, $hUXS_{R236H}$ sediments as a broad peak at a lower value of 3.4 S, close to the theoretical value for the hUXS monomer (3.3 S) (Figure 2A). This confirms our earlier prediction that the *mow* mutation would weaken the dimer.[6] The significant tailing toward high *s* values indicates the presence of a rapid equilibrium with ∼10% dimer in the distribution. At higher protein concentrations (26 μM), the wild-type hUXS distribution shifts to favor a 7.1 S tetramer species in equilibrium with a small amount of 5.0 S dimer (Figure 2B). This concentration-dependent formation of the tetramer has been described in our earlier work.[15] In contrast, a high concentration of $hUXS_{R236H}$ (21 μM) reveals a complex distribution dominated by the 7.1 S tetramer and a new species at 10.2 S. The sedimentation of the larger species closely matches the predicted sedimentation (10.4 S) for the hexamer that we observe in the crystal structure described in the following section. In addition to the tetramer and hexamer,

DOI: 10.1021/bi501357c
Biochemistry 2015, 54, 807−819

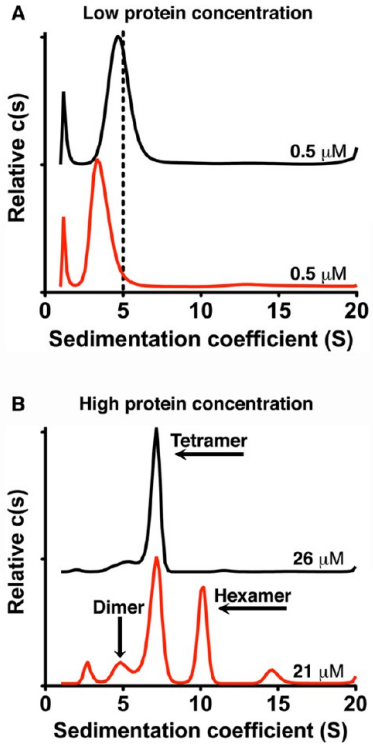

Figure 2. The *mow* mutation alters the hUXS quaternary structure. (A) Sedimentation velocity data modeled as a $c(s)$ distribution. At a concentration of 0.5 μM, wild-type hUXS (black) sediments as a broad peak at 4.6 S. The dashed line represents the predicted s value for the hUXS dimer (5.0 S). Under identical conditions, $hUXS_{R236H}$ (red) sediments as a broad peak at 3.4 S. (B) The distribution of species present in the sedimentation of hUXS (black) and $hUXS_{R236H}$ (red) at a protein concentration of 26 and 21 μM, respectively.

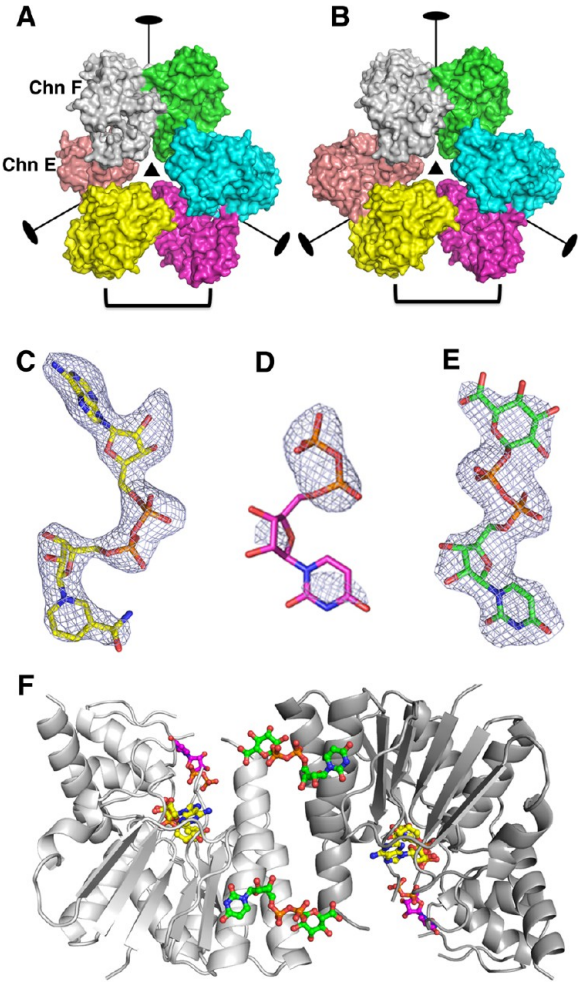

Figure 3. Crystal structures of $hUXS_{R236H}$ and $hUXS_{R236A}$. (A) Surface representation of the hexamer in the $hUXS_{R236H}$ asymmetric unit. The subunits are colored individually, and the 322 symmetry is illustrated. Chains E and F (Chn E and F, respectively) have significantly less surface due to disorder in the crystal structure. (B) Surface representation of the $hUXS_{R236A}$ hexamer with the subunits colored as in panel A. (C–E) Difference density maps (F_o–F_c) calculated at 2.6 Å resolution and contoured at 3σ for $hUXS_{R236A}$. The maps were calculated after omitting the ligands and subjecting the model to simulated annealing. (C) NAD^+ in the active site. (D) UDP modeled in the active site. (E) UDP-GlcA bound to the putative allosteric site in the dimer interface. (F) Cartoon representation of hUXS dimer showing the spatial relationships between the substrate (magenta), cofactor (yellow), and the UDP-GlcA (green) in the second UDP-sugar binding site.

minor amounts of dimer (4.8 S) and a smaller peak (2.7 S) that likely corresponds to a misfolded monomer (Figure 2B) were also observed. Finally, the distribution for $hUXS_{R236H}$ also reveals a small peak at 14.6 S that may indicate the formation of a weak dodecamer (Figure 2B). The s values obtained from rapid equilibrium systems are biased by the mean of the $c(s)$ distribution, meaning that the small deviation in the s value for the dimer (5.0 vs 4.8 S) does not necessarily imply a significant change in the conformation of the complex.[28,29]

Crystal Structures of $hUXS_{R236H}$ and $hUXS_{R236A}$. The *mow* mutant, $hUXS_{R236H}$, was crystallized with UDP and solved using data to 2.86 Å resolution (see Methods and Table 1). The structure contains a hexamer in the asymmetric unit with a predicted s value of 10.4 S, which is consistent with our sedimentation velocity studies (Figure 2B). The hexamer displays 322 symmetry and is built from three hUXS dimers (Figure 3A). In all six chains, the *mow* mutation is located near an extensive region of disorder representing ~20% of the total scattering mass in the crystal (Figure 3A). The disorder includes four structural elements: E_1, E_2, E_3, and E_4 (Table 2). These elements encompass a large fraction of the dimer interface and active site; the consequences of this disorder will be described in a later section. In addition to the E_1, E_2, E_3, and E_4 elements, 52% and 46% of chains E and F, respectively, are disordered in the $hUXS_{R236H}$ crystal structure (Figure 3A). In chain E, the disordered elements also include residues in the nucleotide–sugar binding domain (residues 263–299, 324–363, and 372–399) and the catalytic domain (residues 163–170 and 204–236). In Chain F, large portions of the nucleotide–sugar binding domain (residues 284–301, 324–329, and 343–363) and the catalytic domain (residues 88–94, 110–117, 134–140, 156–169, 195–236, and 253–260) are also disordered. This extensive disorder likely contributes to the poor resolution of the crystals (2.86 Å). To improve the diffraction quality of the crystals, we introduced the R236A substitution in hUXS. The R236A substitution was predicted to disrupt the same electrostatic interactions as R236H while also reducing the steric clashes that would arise from the burial of a bulky imidazole in the dimer interface (Figure 1C,D). Both $hUXS_{R236A}$ and $hUXS_{R236H}$ crystallize as hexamers in similar but nonisomorphous space groups (Table 1). As anticipated, crystals of $hUXS_{R236A}$ in complex with UDP-GlcA diffract to

DOI: 10.1021/bi501357c
Biochemistry 2015, 54, 807–819

Table 2. Disordered Elements in $hUXS_{R236A}$

element	chain A	chain B	chain C	chain D	chain E	chain F
E_1	165−169	166−168	165−169	166−169	163−170	163−169
E_2	207−232	207−232	207−232	207−232	207−232	207−232
E_3	291−294	ordered	ordered	ordered	ordered	288−293
E_4	351−360	352−360	352−361	352−360	352−360	349−360

a higher resolution of 2.64 Å. Despite having a similar crystal lattice, the $hUXS_{R236A}$ structure does not share the extensive disorder seen in chains E and F of $hUXS_{R236H}$ (Figure 3B). However, all six chains of $hUXS_{R236A}$ reveal the same four disordered elements, E_1−E_4, in the dimer interface and active site that we observe in the $hUXS_{R236H}$ structure (Table 2). Despite the disorder in the active site, we see strong, continuous electron density for the bound NAD^+ cofactor (Figure 3C). In contrast, the difference density for the substrate UDP-GlcA is weak and consistent with the loss of packing interactions due to the local unfolding of the active site (Figure 3D). A simulated annealing omit difference map contoured at 3σ shows density for the diphosphate, weak density for the uridine base and ribosyl, and no density for the glucuronic acid. On the basis of this result, we have modeled UDP into the weak density in the active site guided by the position and conformation of the bound UDP observed in wild-type hUXS (PDB entry 2B69) (Figure 3D). In addition to the UDP in the active site, we also observe strong density for a second UDP-GlcA molecule bound in the dimer interface (Figure 3E). We will describe this additional UDP-GlcA binding site in the last section of the results. Because the maximum likelihood estimate[20] of the coordinate errors of the 3.0 and 2.7 Å resolution structures are 0.47 and 0.33 Å, respectively, we have limited our analysis to features of the structures that can be confidently assessed even with near 0.5 Å coordinate uncertainty. These features include (i) quaternary structure, (ii) domain conformation, (iii) mainchain path and secondary structure patterns, (iv) regions of disorder, and (v) the identification of bound nucleotide sugars. All discussion dealing with details such as H-bond geometries and electrostatic interactions is based on the 1.2 Å resolution structure of the hUXS:UDP complex (PDB entry 2B69).

The *mow* Mutation Induces a Local Unfolding of the Dimer Interface and Active Site. The $hUXS_{R236H}$ and $hUXS_{R236A}$ structures share a common region of disorder consisting of four structural elements that represent a large portion of the dimer interface and active site: E_1, E_2, E_3, and E_4 (Table 2, Figure 4). E_1 (residues 163−170) includes the short α-$helix_{165-168}$, which has previously been shown to undergo a disorder-to-order transition upon substrate binding that shields the active site from solvent (Figure 4A).[12] Given the intrinsic flexibility of $helix_{165-168}$, it is possible that the disorder we observe in E_1 is not a direct result of the R236H and R236A substitutions. Because E_1 packs against E_2, it is not unreasonable to assume that the unfolding of the latter element contributes to the greater flexibility of E_1.

In contrast to E_1, the unfolding of E_2 (residues 207−232) is a direct consequence of the *mow* mutation. In wild-type hUXS, R236 is buried in the dimer interface where it forms a salt bridge with E233′ from the adjacent subunit and hydrogen bonds with the main chain carbonyls of residues V205, W219, and V222 (Figure 1D). The E_2 loop contains W219 and V222, and buries all of the R236-mediated electrostatic interactions from solvent (Figure 4A). The R236H and R236A substitutions disrupt this electrostatic network, preventing the E_2 loop from folding and burying the unsatisfied polar and charged groups. E_2 includes residue Y231, the conserved acid/base catalyst in hUXS (Figure 4A).[30,31] This suggests that the unfolding of E_2 will have a negative impact on the enzyme's catalytic activity. Finally, the E_2 loop also interacts with the corresponding E_2' loop across the dimer interface (Figure 4B). A significant interaction involves W219, which is sandwiched between H221′, V222′, and N223′ from the adjacent subunit (Figure 4B,C). Thus, the folding of the E_2 loop in one subunit will facilitate the folding of the symmetry-related E_2' loop (Figure 4B,C). The unfolding of the E_2 loops reduces the size of the dimer interface by 42% (~640 $Å^2$).

In the wild-type enzyme, the folded E_2 loop buttresses the E_4 loop to form an E_2−E_3−E_4 cluster that binds and shields the substrate from bulk solvent (Figure 4A). In $hUXS^{mow}$, the disorder of the E_3 and E_4 loops is likely due to a "domino effect". In this scenario the *mow*-induced unfolding of the E_2 loop destabilizes the E_2−E−E_4 cluster, which unfolds to expose the active site. The unfolding of the cluster is reflected in the disorder observed in the UDP-GlcA molecule bound to the active site (Figure 3D). Despite the increased flexibility, we were able to model the E_3 loop in chains B, C, D, and E of the $hUXS_{R236A}$ structure (Table 2).

The *mow* Mutation Uncovers a Latent Hexameric Complex. In $hUXS_{R236A}$, the hexamer-building interface between adjacent dimers is made up of elements from both the catalytic and nucleotide−sugar binding domains and buries an area of 670 ± 18 $Å^2$ (Figure 5A). In total, 40 residues are partially or completely buried, including 16 hydrogen-bonding pairs and two salt bridges (Table 3). The predominantly polar nature of the interface suggests that it is likely to be weak, consistent with our sedimentation velocity studies that show that the hexamer forms only at relatively high protein concentration (~21 μM) (Figure 2B). Most members of the SDR family form dimers or tetramers.[13,14] To our knowledge, the only SDR enzymes identified as hexameric are the UDP-GlcNAc-inverting 4,6-dehydratases from *Staphylococcus aureus* (CapE) and *Helicobacter pylori* (FlaA1).[32,33] Despite the fact that hUXS shares low sequence identities with CapE (21%) and FlaA1 (16%), the structures are highly conserved; hUXS superimposes 207 Cα atoms onto CapE and 204 Cα atoms onto FlaA1 with RMSDs of 1.9 and 2.0 Å, respectively (Figures 5B and S1 in the Supporting Information). The similarity between the *mow*-induced hUXS hexamer and the CapE and FlaA1 complexes is striking (Figure 5C). These hexamers share the same interaction surface between adjacent dimers with only minor structural changes (Figure 5B). Specifically in UXS, structural elements α2, β3, α3, and α11 have shifted relative to the CapE and FlaA1 structures.

To form the hexamer, the $hUXS_{R236H}$ and $hUXS_{R236A}$ dimers are "bent" relative to wild-type hUXS (Figure 6). The bending of the dimer is a consequence of a small rigid-body rotation of the individual subunits about an axis located in the dimer interface (Figure 6A). The rotation is directed toward the

DOI: 10.1021/bi501357c
Biochemistry 2015, 54, 807−819

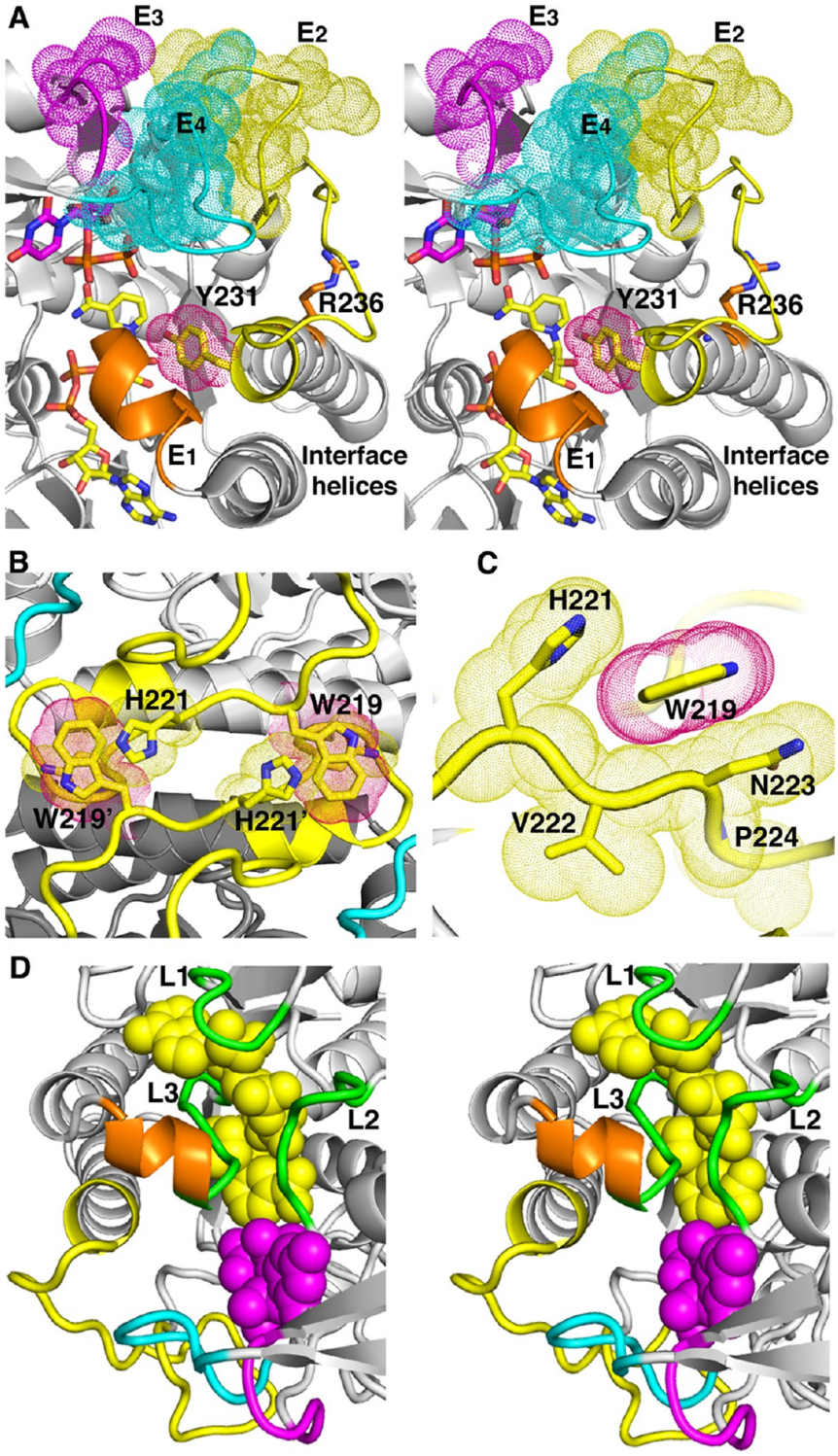

Figure 4. The *mow* mutation induces the unfolding of the hUXS active site and dimer interface. (A) Stereodiagram depicting the interactions of the structural elements E_1 (orange), E_2 (yellow), E_3 (magenta), and E_4 (cyan) in wild-type hUXS conformation (PDB entry 2B69). These interactions are lost due to local unfolding in $hUXS_{R236A}$. The interactions between elements are indicated by van der Waals surfaces (dots) of elements E_2–E_4. The site of the *mow* mutation R236, NAD^+ (yellow), and UDP (magenta) are shown. The catalytic tyrosine (Y231) is shown with a van der Waals surface (pink dots). Y168 from element E_1 packs against Y231 from E_2, but this interaction is not shown for reasons of clarity. (B) The wild-type hUXS dimer interface showing packing interactions between loop E_2 (yellow) from the two different subunits. Dimer subunits are colored light and dark gray. The side chains of interacting residues H221 and W219 are shown using van der Waals radii (yellow and pink dots, respectively). Residues from chain B are labeled H221′ and W219′, respectively. (C) View of the dimer interface interactions between W219 and the loop containing residues 221–224 in wild-type hUXS. (D) Stereodiagram showing the active site of wild-type hUXS (gray, PDB entry 2B69) with NAD^+ (yellow) and UDP (magenta) shown as spheres. The loops L1, L2, and L3 (green) bind the cofactor.[12] All other elements are colored as in panel A.

DOI: 10.1021/bi501357c
Biochemistry 2015, 54, 807–819

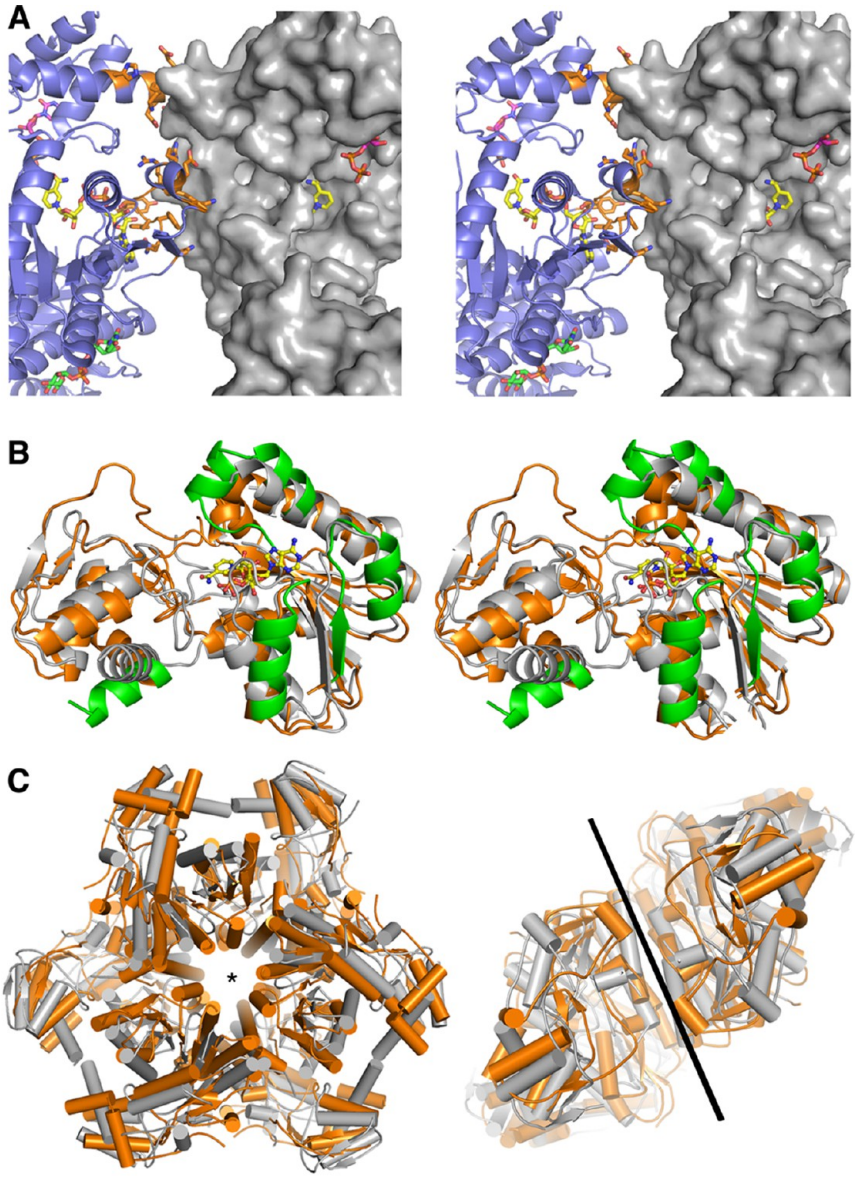

Figure 5. Hexamer-building interfaces in hUXS and related enzymes. (A) Stereodiagram of the hexamer-building interface between two $hUXS_{R236A}$ dimers (blue cartoon and gray surface, respectively). Buried or interacting residues are shown as sticks (orange with atomic colors). NAD^+ (yellow) and UDP (magenta) in the active site and UDP-GlcA (green) in the second UDP-sugar binding site are also shown. Note that the surface rendering shows that the active site is exposed to solvent. (B) Superposition of monomers of $hUXS_{R236A}$ (light gray, PDB entry 4LK3) and CapE (orange, PDB entry 3VVC). The structural elements of the hexamer interface α2, β3, α3 and α11 in $hUXS_{R236A}$ have shifted relative to the CapE elements (green). (C) Cartoon representation of the superposition of the *mow*-induced hexamer $hUXS_{R236A}$ (light gray, PDB entry 4LK3) and hexameric SDR enzyme, UDP-GlcNAc-inverting 4,6-dehydratase from *Staphylococcus aureus* (CapE, orange, PDB entry 3VVC) illustrating that these structures are highly conserved. The top and side views of the superposed hexamers are depicted.

unfolded regions of the dimer interface. In $hUXS_{R236H}$, dimers formed by chains C and D and chains E and F are "bent" by 5.4° and 3.1°, respectively. The remaining $hUXS_{R236H}$ dimer formed by chains A and B resembles the wild-type conformation. This variability in the rotation angles suggests that the partial unfolding of the interface has introduced flexibility into the dimer as well. In contrast, all dimers of the $hUXS_{R236A}$ structure reveal a consistent 4.2° ± 0.2° rotation angle.

The *mow* Mutation Favors the Formation of the Abortive Complex. We have previously shown that hUXS can undergo an abortive catalytic cycle that releases the reaction intermediates NADH and UDP-4-keto-Xyl (Figure 1B).[12] The resulting apoenzyme can be rescued with exogenous NAD^+ to produce the reaction intermediates in addition to the final product, UDP-Xyl (Figure 7A). As expected, the $hUXS_{R236H}$ and $hUXS_{R236A}$ constructs do not produce UDP-Xyl (Figure 7A). However, they do produce and release the reaction intermediates (Figure 7). The crystal structures of $hUXS_{R236H}$ and $hUXS_{R236A}$ show that the conserved acid−base catalyst Y231 is disordered due to the local unfolding of the E_2 loop in the active site (Figure 4A). To see if the loss of Y231 could explain the catalytic defect in $hUXS_{R236H}$ and $hUXS_{R236A}$, we introduced the Y231F substitution in hUXS ($hUXS_{Y231F}$). $hUXS_{Y231F}$ undergoes only the abortive catalytic cycle, albeit at a rate similar to the wild-type enzyme (Figure 7).

Identification of a Unique Nucleotide-Sugar Binding Site in the Dimer Interface. In addition to the weakly

DOI: 10.1021/bi501357c
Biochemistry 2015, 54, 807−819

Table 3. The Hexamer-Building Interface

electrostatic interactions between chains[a]	buried residues[a]	
Asn120 (Nδ2) ↔ Asn142 (Oδ1)	Asn120	Gly134
Phe121 (O) ↔ Lys126 (Nζ)	Phe121	Asn142
Phe122 (O) ↔ Lys126 (Nζ)	Phe122	Tyr170
Gly124 (O) ↔ Lys126 (Nζ)	Thr123	His389
Arg127 (Nη2) ↔ Glu130 (Oε1)[b]	Gly124	Lys393
Arg127 (Nη1) ↔ Tyr397 (OηH)	Arg125	Glu394
Asn142 (Nδ2) ↔ Asn142 (Oδ1)	Lys126	Glu396
Asn142 (Nδ2) ↔ Asn120 (O)	Arg127	Tyr397
Glu394 (Oε2) ↔ Tyr397 (OηH)	Glu130	Gln389
	Ile133	Ala399

[a]The application of 2-fold symmetry doubles these interactions within each interface. [b]Salt bridge.

ordered UDP-GlcA located in the active site, a second molecule of UDP-GlcA is bound in a well-defined pocket on the surface of the protein (Figure 8A). The distinguishing feature of this pocket is a loop (residues 149−151) conserved only in the UXS enzymes of the SDR family; the homologous bacterial UDP-glucuronic acid decarboxylase (ArnA) and all other SDR family enzymes conserve an α-helix in place of $Loop_{149-151}$ (Figure 8B). The uridine base of UDP forms two hydrogen bonds with the mainchain of L149 in $Loop_{149-151}$, and accepts a proton from the guanidinium of R192 (Figures 8A and S2 in the Supporting Information). The uridine base is sandwiched between packing interactions with P148 and Y150 on the top and by a complementary surface formed by G188, L189, and N185 on the bottom. The pyrophosphate of UDP-GlcA interacts with Y245 and K177′ from the adjacent subunit. The O2 hydroxyl of GlcA accepts a proton from K191 while O3 forms hydrogen bonds with Q248 and E249. The carboxylate of GlcA makes two hydrogen bonds with N171′ and K177′ from the neighboring subunit. Finally, residues L184, Y245, I173′, and K174′ form a complementary surface that packs against the glucuronic acid moiety.

DISCUSSION

The *mow* Mutation Uncovers a Latent Hexamer-Forming Potential. The *mow* phenotype in zebrafish is

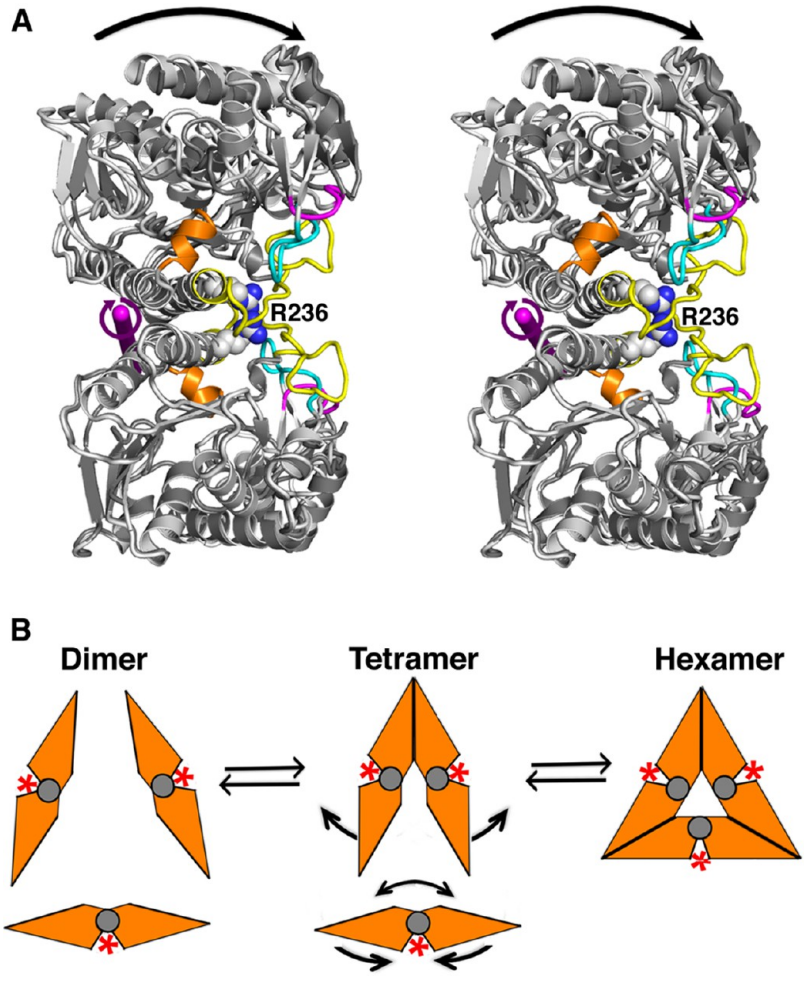

Figure 6. The *mow*-induced rotation of the hUXS dimer interface facilitates hexamer formation. (A) Stereodiagram of the superposition of wild-type hUXS (light gray, PDB entry 2B69) and $hUXS_{R236A}$ (dark gray) dimers illustrating the rotation (arrow) of the subunits about an axis (magenta rod) located in the dimer interface. The rotation is toward the disordered E_1 (orange), E_2 (yellow), E_3 (cyan), and E_4 (magenta) structural elements in $hUXS_{R236A}$. The site of the *mow* mutation (R236, spheres) is labeled. (B) Model depicting the dependence of $hUXS^{mow}$ hexamer formation on dimer conformation. Two $hUXS^{mow}$ dimers (orange polygons) associate to form a tetramer. To form the hexamer, the dimers must rotate about the interface (gray circle) in the direction of the curved arrows. The *mow* mutation (red asterisk) introduces the interface flexibility needed to facilitate this rotation.

DOI: 10.1021/bi501357c
Biochemistry 2015, 54, 807−819

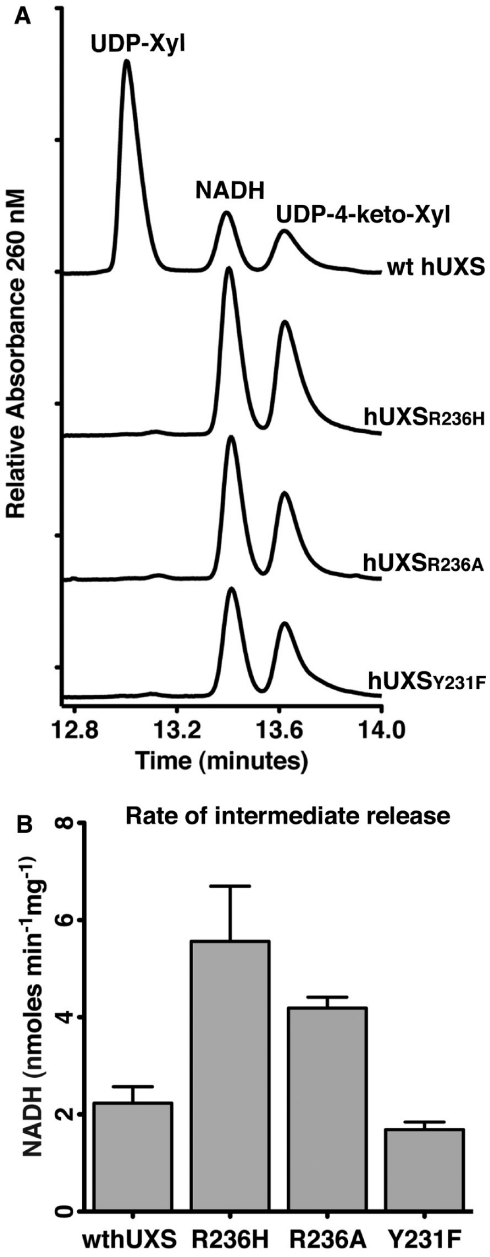

Figure 7. The *mow* mutation favors the abortive catalytic cycle. (A) Capillary zone electrophoresis of reaction products of wild-type hUXS and its variants ($hUXS_{R236H}$, $hUXS_{R236A}$, and $hUXS_{Y231F}$) shows that the mutant constructs do not produce UDP-Xyl. However, all constructs undergo the abortive catalytic cycle to produce UDP-4-keto-Xyl and NADH. (B) Graph comparing the rates of reaction intermediate release by hUXS and its variants. All readings were conducted in triplicate. The error bars depict standard deviation.

characterized by craniofacial and other developmental defects caused by reduced levels of proteoglycans.[6] We have previously shown that the *mow* phenotype is caused by an inactivating missense mutation in the UXS gene (R236H), which prevents the synthesis of the essential substrate required for proteoglycan biosynthesis.[6] Because R236 is buried in the dimer interface and contributes to several favorable electrostatic interactions, we speculated that the loss of activity was due to the disruption of the UXS dimer (Figure 1C,D).[6] We have also shown that hUXS dimers undergo a concentration-dependent association to form a tetramer, which represents the catalytically important oligomeric state of hUXS.[15] This result prompted us to examine the structural consequences of the *mow* mutation in detail. Here we show that the R236H substitution weakens the dimeric complex as expected (Figure 2A). However, a higher concentration of $hUXS_{R236H}$ favors the formation of the dimer and tetramer as well as a new hexameric complex (Figure 2B). The crystal structure of $hUXS_{R236H}$ confirms the hexamer, but because of the extensive disorder the crystals diffracted weakly to 2.86 Å resolution. The poor resolution may have been due to bad contacts resulting from the replacement of the arginine side chain with a bulky imidazole. In an attempt to improve crystal quality, we introduced the R236A substitution to disrupt the same electrostatic interactions, albeit with a more modest steric effect. The $hUXS_{R236H}$ and $hUXS_{R236A}$ constructs crystallize as hexamers in similar but nonisomorphous unit cells, with the latter diffracting to 2.6 Å resolution. The two structures share the same unfolding of a significant portion of the active site and the dimer interface, representing ~20% of the total scattering mass (Figure 4A). This is not surprising given that the burial of an unsatisfied charge or polar group is often associated with the local unfolding or conformational changes in the protein structure to expose that group to solvent.[34] The polar nature of the hexamer-building interface suggests that it is likely to be unstable and will only form under crowding conditions (Table 3). This interpretation is consistent with the sedimentation velocity studies that show that the hexamer is formed at high protein concentrations (Figure 2). The $hUXS_{R236H}$ and $hUXS_{R236A}$ structures also reveal the basis of hexamer formation. The unfolding of E_1–E_4 permits a ~4° rotation of the subunits about an axis located in the interface (Figure 6A). This rotation is essential for three hUXS dimers to associate into the hexamer (Figure 6B). The variability in the *mow*-induced rotation (0–5.4°) in the $hUXS_{R236H}$ structure suggests that the dimer interface is flexible. The increased flexibility explains the dimer–tetramer–hexamer distribution observed in the sedimentation velocity experiments of $hUXS^{mow}$ (Figure 2B). A priori, one would assume that a hexamer with three interacting surfaces would be more stable than a tetramer with a single contact. However, the additional conformational freedom due to the flexible interface could preferentially weaken the hexamer. This explains why a significant amount of tetramer is observed at high protein concentrations (Figure 2B).

In wild-type hUXS the hexamer-building interface is still exposed and can interact, but only a tetramer has been observed in solution (Figure 2B).[15] This is likely due to the inability of the wild-type tetramer to accommodate a third dimer in the absence of the *mow*-induced rotations (Figure 6B). Thus, we believe that the wild-type hUXS tetramer seen here and in previous studies[15] is built using the same dimer–dimer interface that produces the *mow* hexamer (Figure 5A). The observation that the active sites in the tetramer and hexamer are not occluded suggests that the higher order oligomers are active. This hypothesis is consistent with our earlier work showing that wild-type hUXS tetramer is six times more active than the dimer (Figure 4).[15] Thus, the persistence of the hexamer-building interface in hUXS may be due to the functional significance of a tetramer with higher activity. The conservation of this oligomeric interface between hUXS and deeply divergent SDR enzymes also suggests that the ancestral UXS enzyme may have been a hexamer (Figure 5B).

The *mow* Phenotype is Due to an Abortive Catalytic Cycle. Next, we turned our attention to the molecular basis for

DOI: 10.1021/bi501357c
Biochemistry 2015, 54, 807–819

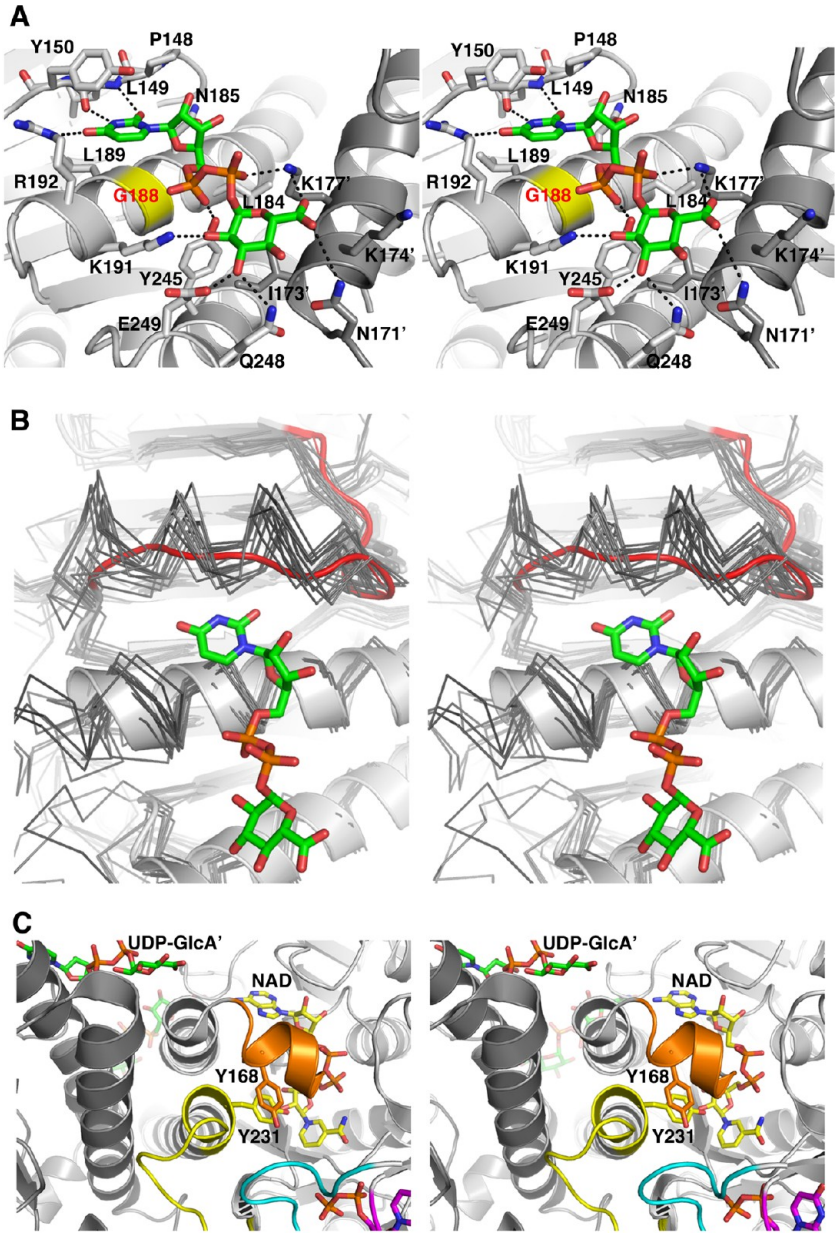

Figure 8. UDP-GlcA bound to a second UDP-sugar binding site in the hUXS dimer interface. (A) Stereodiagram showing hydrogen bonds (dashed lines) and the packing interactions between bound UDP-GlcA (green sticks) and the second UDP-sugar binding site in the $hUXS_{R236A}$ dimer interface. Individual chains in the dimer interface are colored light gray and dark gray. Interacting residues from the neighboring subunit are denoted with a prime (′). The conserved G188 (yellow surface) is identified with red letters. (B) Stereodiagram showing the evolutionary conservation of the UDP binding loop (red). (C) Stereodiagram illustrating the relationship between the second UDP-sugar binding site and the active site. A bound UDP-sugar (UDP-GlcA′) could influence the packing of the flexible active site element E_1 ($helix_{165–168}$, colored orange). Loop E_2 (yellow) and the active site acid/base catalyst Tyr231 are also depicted. SDR structures used in panel (B) with PDB entry codes in parentheses: human GDP-mannose 4,6-dehydratase (1T2A), *E. coli* dTDP-glucose 4,6-dehydratase (1BXK), *Salmonella enterica* dTDP-glucose 4,6-dehydratase (1KEU),[42] *Helicobacter pylori* UDP-GlcNAC 4,6-dehydratase (2GN9),[33] *Arabidopsis thaliana* GDP-mannose 4,6-dehydratase (1N7G),[43] *Yersinia pseudotuberculosis* CDP-glucose 4,6-dehydratase (1RKX),[44] *Streptococcus suis* dTDP-glucose 4,6-dehydratase (1OC2),[45] *Bordetella bronchiseptica* putative SDR (2Q1T),[46] *Trypanosoma brucei* UDP-galactose 4-epimerase (2CNB),[47] human UDP-galactose 4-epimerase (1EK5),[48] *Bacillus anthracis* UDP-glucose 4-epimerase (2C20) and *Arabidopsis thaliana* sulfolipid biosynthesis protein (1QRR).[49]

the catalytic defect in $hUXS_{R236H}$ and $hUXS_{R236A}$ (Figure 7A). We have previously shown that wild-type hUXS can undergo an abortive catalytic cycle that releases the reaction intermediates UDP-4-keto-Xyl and NADH, and that the resulting apoenzyme can be rescued with exogenous NAD^+ (Figure 1B).[12] The rate-limiting step in the release of the intermediates is a slow conformational change that exposes the active site to solvent.[12] Here we show that $hUXS_{R236H}$ and $hUXS_{R236A}$ only undergo the abortive cycle, and cannot produce UDP-Xyl (Figure 7A). The loss of activity is most likely due to the local unfolding observed in the crystal structures of $hUXS_{R236H}$ and $hUXS_{R236A}$ (Figure 4). The disordered elements include residue Y231 in the active site (Figure 4A). Y231 is one of three conserved catalytic residues in the SDR family of enzymes, and acts as an acid/base catalyst in the reaction mechanism.[30] To see if the catalytic defect in $hUXS_{R236H}$ and $hUXS_{R236A}$ was simply due to the loss

DOI: 10.1021/bi501357c
Biochemistry 2015, 54, 807–819

of the Y231 hydroxyl, we introduced the Y231F substitution into the wild-type enzyme. As previously reported,[31] $hUXS_{Y231F}$ can oxidize UDP-GlcA to UDP-4-keto-Xyl, but cannot reduce the intermediates to produce UDP-Xyl (Figure 7A). This suggests that the molecular basis for the *mow* phenotype in zebrafish is a mutation-induced misfolding of the active site that displaces an essential catalytic tyrosine.

The $hUXS_{R236H}$ and $hUXS_{R236A}$ crystal structures suggest that the unfolding of loops E_1-E_4 will remove stabilizing packing interactions from the NADH-retaining loops (L1−L3) and facilitate the release of the intermediates by exposing the sugar substrate (Figure 4D). To test this hypothesis, we examined the release rate of the reaction intermediates. The bifurcated reaction mechanism of wild-type hUXS complicates a direct comparison with $hUXS_{R236H}$ and $hUXS_{R236A}$ (Figure 1B); in the wild-type enzyme the release of the intermediates competes with UDP-Xyl synthesis. We chose the $hUXS_{Y231F}$ construct to analyze the effect of the *mow*-induced unfolding on the release of reaction intermediates for the following two reasons. First, $hUXS_{Y231F}$ produces only the reaction intermediates. Second, the Y231F substitution is unlikely to disrupt the structure. In fact, the analogous Y to F substitution in the closely related enzyme UDP-galactose-4-epimerase has no significant effect on the protein structure.[30] Our results show that both $hUXS_{R236H}$ and $hUXS_{R236A}$ release the ketose intermediate ∼2−2.5 times faster than $hUXS_{Y231F}$, consistent with the hypothesis that the misfolded active site facilitates the release of the reaction intermediates (Figure 7B).

Evidence for an Additional Nucleotide Binding Site in hUXS. We have identified a second UDP-GlcA binding site located in the dimer interface of all six chains of the $hUXS_{R236H}$ and $hUXS_{R236A}$ hexamers (Figures 3E,8). This is the same site that was previously shown to contain a molecule of UDP in the wild-type hUXS crystal structure.[31] In that earlier work, Eixelsberger et al. dismissed the interaction as a nonspecific crystal contact. Given the different crystallization conditions and unique packing environments of the wild-type and $hUXS^{mow}$ structures, our observation of a UDP-sugar bound in the same site as the UDP in wild-type hUXS is good evidence of a specific interaction. Additional evidence for a second nucleotide sugar-binding site can be seen in the evolution of hUXS, a member of the SDR family of enzymes.[13] All other SDR enzymes conserve an α-helix in place of the nucleotide-binding $Loop_{149-151}$ in UXS, suggesting the loop was under selective pressure (Figure 8B). In addition, Gly188 is conserved in all UXS enzymes, and contributes a key packing interaction to the bound uridine base (Figure 8A). What makes this specific interaction interesting is the fact that Gly188 is located in α-$helix_{181-192}$, and glycine is known to be the most helix destabilizing amino acid.[35,36] Because Gly188 is solvent-exposed (in the absence of UDP-binding), it should be free to diverge to an amino acid with a more favorable helix-forming propensity. However, the presence of a C_β atom would clash with the uridine base and inhibit the binding of a UDP-sugar ligand (Figure 8A). The conservation implies that Gly188 has been subjected to positive selective pressure during evolution. It is tempting to speculate that this site may be involved in the allosteric regulation of the enzyme. Allostery in hUXS is not without precedent. UXS from chicken and wheat germ has been shown to display sigmoidal kinetics and is believed to be allosterically activated by UDP-GlcA and inhibited by UDP-Xyl.[37,38] In fact, the binding site is located near the dynamic $helix_{165-168}$ in the active site of the adjacent subunit, suggesting a means of regulating activity (Figure 8C). Although the structural evidence supports our identification of a second nucleotide sugar-binding site in hUXS, we are somewhat at a loss to conclusively identify the authentic ligand. Even though UDP-GlcA is well ordered in our structures, it is possible that the site is specific for a different UDP-sugar ligand and the relatively high concentrations of ligand used during crystallization drove the UDP-GlcA binding. Future studies will focus on the function of this binding site and the identity of the authentic UDP-sugar ligand.

■ ASSOCIATED CONTENT

Supporting Information

Structure-based sequence alignment of $hUXS_{R236A}$ (4LK3) with two SDR enzymes that are known to be hexameric: UDP-GlcNAc-inverting 4,6-dehydratases from *S. aureus* (3VVC) and from *H. pylori* (2GN4).[33] Also, a Ligplot of hydrogen bonds and packing interactions between $hUXS_{R236A}$ and the UDP-GlcA molecule bound in the putative allosteric binding site. This material is available free of charge via the Internet at http://pubs.acs.org.

Accession Codes

The atomic coordinates and structure factors for UXS_{R236H} and UXS_{R236A} have been deposited in the Protein Data Bank under entries 4M55 and 4LK3, respectively.

■ AUTHOR INFORMATION

Corresponding Author

*Phone: 706-583-0304, Fax: 706-542-1738, email: zac@bmb.uga.edu.

Present Addresses

[†]R.M.W.: The Department of Biophysics, University of Texas Southwestern Medical Center, 5323 Harry Hines Blvd, Dallas, TX 75390.

[‡]S.J.P.: The Department of Chemistry and Biochemistry, Kennesaw State University, 1000 Chastain Rd, Kennesaw, GA 30144.

[§]W.W.H.: The School of Medicine, Johns Hopkins University, Baltimore, MD 21218

Funding

Funding from the University of Georgia Research Alliance and the American Cancer Society (Grant RSG0918401DMC) to Z.A.W. is gratefully acknowledged.

Notes

The authors declare no competing financial interest.

■ ACKNOWLEDGMENTS

We thank P. Andrew Karplus for helpful discussions and insights. We also thank the SER-CAT beamline personnel (Advanced Photon Source, Argonne National Lab, Argonne, IL) for help with the data collection.

■ ABBREVIATIONS

UDP, uridine diphosphate; hUXS, human UDP-xylose synthase; UDP-GlcA, UDP−α-D-glucuronic acid; UDP-4-keto-Xyl, UDP−α-D-4-keto-xylose; UDP-Xyl, UDP−α-D-xylose; CZE, capillary zone electrophoresis; *mow*, *man o' war*; GAG, glycosaminoglycan; SDR, short-chain dehydrogenase

■ REFERENCES

(1) Silbert, J. E., and Sugumaran, G. (2002) Biosynthesis of chondroitin/dermatan sulfate. *IUBMB Life 54*, 177−186.

DOI: 10.1021/bi501357c
Biochemistry 2015, 54, 807−819

(2) Fuster, M. M., and Esko, J. D. (2005) The sweet and sour of cancer: glycans as novel therapeutic targets. *Nat. Rev. Cancer 5*, 526−542.
(3) Lamoureux, F., Baud'huin, M., Duplomb, L., Heymann, D., and Redini, F. (2007) Proteoglycans: key partners in bone cell biology. *BioEssays 29*, 758−771.
(4) Bai, X., Zhou, D., Brown, J. R., Crawford, B. E., Hennet, T., and Esko, J. D. (2001) Biosynthesis of the linkage region of glycosaminoglycans: cloning and activity of galactosyltransferase II, the sixth member of the beta 1,3-galactosyltransferase family (beta 3GalT6). *J. Biol. Chem. 276*, 48189−48195.
(5) Sugahara, K., and Kitagawa, H. (2002) Heparin and heparan sulfate biosynthesis. *IUBMB Life 54*, 163−175.
(6) Eames, B. F., Singer, A., Smith, G. A., Wood, Z. A., Yan, Y. L., He, X., Polizzi, S. J., Catchen, J. M., Rodriguez-Mari, A., Linbo, T., Raible, D. W., and Postlethwait, J. H. (2010) UDP xylose synthase 1 is required for morphogenesis and histogenesis of the craniofacial skeleton. *Dev. Biol. 341*, 400−415.
(7) Esko, J. D., Rostand, K. S., and Weinke, J. L. (1988) Tumor formation dependent on proteoglycan biosynthesis. *Science 241*, 1092−1096.
(8) Belting, M., Borsig, L., Fuster, M. M., Brown, J. R., Persson, L., Fransson, L. A., and Esko, J. D. (2002) Tumor attenuation by combined heparan sulfate and polyamine depletion. *Proc. Natl. Acad. Sci. U.S.A. 99*, 371−376.
(9) Kearns, A. E., Vertel, B. M., and Schwartz, N. B. (1993) Topography of glycosylation and UDP−xylose production. *J. Biol. Chem. 268*, 11097−11104.
(10) Hwang, H. Y., and Horvitz, H. R. (2002) The *Caenorhabditis elegans* vulval morphogenesis gene sqv-4 encodes a UDP-glucose dehydrogenase that is temporally and spatially regulated. *Proc. Natl. Acad. Sci. U.S.A. 99*, 14224−14229.
(11) Moriarity, J. L., Hurt, K. J., Resnick, A. C., Storm, P. B., Laroy, W., Schnaar, R. L., and Snyder, S. H. (2002) UDP−glucuronate decarboxylase, a key enzyme in proteoglycan synthesis: cloning, characterization, and localization. *J. Biol. Chem. 277*, 16968−16975.
(12) Polizzi, S. J., Walsh, R. M., Jr., Peeples, W. B., Lim, J. M., Wells, L., and Wood, Z. A. (2012) Human UDP-alpha-D-xylose synthase and *Escherichia coli* ArnA conserve a conformational shunt that controls whether xylose or 4-keto-xylose is produced. *Biochemistry 51*, 8844−8855.
(13) Field, R. A., and Naismith, J. H. (2003) Structural and mechanistic basis of bacterial sugar nucleotide-modifying enzymes. *Biochemistry 42*, 7637−7647.
(14) Kavanagh, K. L., Jornvall, H., Persson, B., and Oppermann, U. (2008) Medium- and short-chain dehydrogenase/reductase gene and protein families: the SDR superfamily: functional and structural diversity within a family of metabolic and regulatory enzymes. *Cell. Mol. Life Sci. 65*, 3895−3906.
(15) Polizzi, S. J., Walsh, R. M., Jr., Le Magueres, P., Criswell, A. R., and Wood, Z. A. (2013) Human UDP-alpha-D-xylose synthase forms a catalytically important tetramer that has not been observed in crystal structures. *Biochemistry 52*, 3888−3898.
(16) Kabsch, W. (2010) XDS. *Acta Crystallogr., Sect. D 66*, 125−132.
(17) Brunger, A. T. (1997) Free *R* value: Cross-validation in crystallography. *Methods Enzymol. 277*, 366−396.
(18) Karplus, P. A., and Diederichs, K. (2012) Linking crystallographic model and data quality. *Science 336*, 1030−1033.
(19) McCoy, A. J., Grosse-Kunstleve, R. W., Adams, P. D., Winn, M. D., Storoni, L. C., and Read, R. J. (2007) Phaser crystallographic software. *J. Appl. Crystallogr. 40*, 658−674.
(20) Adams, P. D., Afonine, P. V., Bunkoczi, G., Chen, V. B., Davis, I. W., Echols, N., Headd, J. J., Hung, L. W., Kapral, G. J., Grosse-Kunstleve, R. W., McCoy, A. J., Moriarty, N. W., Oeffner, R., Read, R. J., Richardson, D. C., Richardson, J. S., Terwilliger, T. C., and Zwart, P. H. (2010) PHENIX: a comprehensive Python-based system for macromolecular structure solution. *Acta Crystallogr., Sect. D: Biol. Cryst. 66*, 213−221.
(21) Emsley, P., and Cowtan, K. (2004) Coot: model-building tools for molecular graphics. *Acta Crystallogr., Sect. D.: Biol. Cryst. 60*, 2126−2132.
(22) Hayward, S., and Lee, R. A. (2002) Improvements in the analysis of domain motions in proteins from conformational change: DynDom version 1.50. *J. Mol. Graphics Modell. 21*, 181−183.
(23) Krissinel, E., and Henrick, K. (2007) Inference of macromolecular assemblies from crystalline state. *J. Mol. Biol. 372*, 774−797.
(24) Bruns, C. M., Hubatsch, I., Ridderstrom, M., Mannervik, B., and Tainer, J. A. (1999) Human glutathione transferase A4−4 crystal structures and mutagenesis reveal the basis of high catalytic efficiency with toxic lipid peroxidation products. *J. Mol. Biol. 288*, 427−439.
(25) Laue, T. M., Shah, B. D., Ridgeway, T. M., and Pelletier, S. L. (1992) in Computer-aided interpretation of analytical sedimentation data for proteins, *Analytical Ultracentrifugation in Biochemistry and Polymer Science* (Harding, S. E., Rowe, A. J., and Horton, J. C., Eds.) pp 90−125, The Royal Society of Chemistry, Cambridge, U.K.
(26) Brown, P. H., and Schuck, P. (2006) Macromolecular size-and-shape distributions by sedimentation velocity analytical ultracentrifugation. *Biophys. J. 90*, 4651−4661.
(27) Ortega, A., Amoros, D., and Garcia de la Torre, J. (2011) Prediction of hydrodynamic and other solution properties of rigid proteins from atomic- and residue-level models. *Biophys. J. 101*, 892−898.
(28) Schuck, P. (2003) On the analysis of protein self-association by sedimentation velocity analytical ultracentrifugation. *Anal. Biochem. 320*, 104−124.
(29) Zhao, H., Balbo, A., Brown, P. H., and Schuck, P. (2011) The boundary structure in the analysis of reversibly interacting systems by sedimentation velocity. *Methods 54*, 16−30.
(30) Liu, Y., Thoden, J. B., Kim, J., Berger, E., Gulick, A. M., Ruzicka, F. J., Holden, H. M., and Frey, P. A. (1997) Mechanistic roles of tyrosine 149 and serine 124 in UDP-galactose 4-epimerase from *Escherichia coli*. *Biochemistry 36*, 10675−10684.
(31) Eixelsberger, T., Sykora, S., Egger, S., Brunsteiner, M., Kavanagh, K. L., Oppermann, U., Brecker, L., and Nidetzky, B. (2012) Structure and mechanism of human UDP−xylose synthase: evidence for a promoting role of sugar ring distortion in a three-step catalytic conversion of UDP-glucuronic acid. *J. Biol. Chem. 287*, 31349−31358.
(32) Miyafusa, T., Caaveiro, J. M., Tanaka, Y., Tanner, M. E., and Tsumoto, K. (2013) Crystal structure of the capsular polysaccharide synthesizing protein CapE of *Staphylococcus aureus*. *Biosci. Rep. 33*, e00043.
(33) Ishiyama, N., Creuzenet, C., Miller, W. L., Demendi, M., Anderson, E. M., Harauz, G., Lam, J. S., and Berghuis, A. M. (2006) Structural studies of FlaA1 from *Helicobacter pylori* reveal the mechanism for inverting 4,6-dehydratase activity. *J. Biol. Chem. 281*, 24489−24495.
(34) Blaber, M., Lindstrom, J. D., Gassner, N., Xu, J., Heinz, D. W., and Matthews, B. W. (1993) Energetic cost and structural consequences of burying a hydroxyl group within the core of a protein determined from Ala→Ser and Va→Thr substitutions in T4 lysozyme. *Biochemistry 32*, 11363−11373.
(35) Chakrabartty, A., Kortemme, T., and Baldwin, R. L. (1994) Helix propensities of the amino acids measured in alanine-based peptides without helix-stabilizing side-chain interactions. *Protein Sci. 3*, 843−852.
(36) Pace, C. N., and Scholtz, J. M. (1998) A helix propensity scale based on experimental studies of peptides and proteins. *Biophys. J. 75*, 422−427.
(37) John, K. V., Schutzbach, J. S., and Ankel, H. (1977) Separation and allosteric properties of two forms of UDP−glucuronate carboxy-lyase. *J. Biol. Chem. 252*, 8013−8017.
(38) John, K. V., Schwartz, N. B., and Ankel, H. (1977) UDP−glucuronate carboxy-lyase in cultured chondrocytes. *J. Biol. Chem. 252*, 6707−6710.
(39) Diederichs, K., and Karplus, P. A. (1997) Improved *R*-factors for diffraction data analysis in macromolecular crystallography. *Nat. Struct. Biol. 4*, 269−275.

DOI: 10.1021/bi501357c
Biochemistry 2015, 54, 807−819

(40) Weiss, M. S., and Hilgenfeld, R. (1997) On the use of the merging *R* factor as a quality indicator for X-ray data. *J. Appl. Crystallogr. 30*, 203−205.
(41) Weiss, M. S. (2001) Global indicators of X-ray data quality. *J. Appl. Crystallogr. 34*, 130−135.
(42) Allard, S. T., Beis, K., Giraud, M. F., Hegeman, A. D., Gross, J. W., Wilmouth, R. C., Whitfield, C., Graninger, M., Messner, P., Allen, A. G., Maskell, D. J., and Naismith, J. H. (2002) Toward a structural understanding of the dehydratase mechanism. *Structure 10*, 81−92.
(43) Mulichak, A. M., Bonin, C. P., Reiter, W. D., and Garavito, R. M. (2002) Structure of the MUR1 GDP-mannose 4,6-dehydratase from *Arabidopsis thaliana*: implications for ligand binding and specificity. *Biochemistry 41*, 15578−15589.
(44) Vogan, E. M., Bellamacina, C., He, X., Liu, H. W., Ringe, D., and Petsko, G. A. (2004) Crystal structure at 1.8 A resolution of CDP-D-glucose 4,6-dehydratase from *Yersinia pseudotuberculosis*. *Biochemistry 43*, 3057−3067.
(45) Beis, K., Allard, S. T., Hegeman, A. D., Murshudov, G., Philp, D., and Naismith, J. H. (2003) The structure of NADH in the enzyme dTDP-D-glucose dehydratase (RmlB). *J. Am. Chem. Soc. 125*, 11872−11878.
(46) King, J. D., Harmer, N. J., Preston, A., Palmer, C. M., Rejzek, M., Field, R. A., Blundell, T. L., and Maskell, D. J. (2007) Predicting protein function from structure−the roles of short-chain dehydrogenase/reductase enzymes in *Bordetella* O-antigen biosynthesis. *J. Mol. Biol. 374*, 749−763.
(47) Alphey, M. S., Burton, A., Urbaniak, M. D., Boons, G. J., Ferguson, M. A., and Hunter, W. N. (2006) *Trypanosoma brucei* UDP-galactose-4′-epimerase in ternary complex with NAD+ and the substrate analogue UDP-4-deoxy-4-fluoro-alpha-D-galactose. *Acta Crystallogr., Sect. F: Struct. Biol. Cryst. Commun. 62*, 829−834.
(48) Thoden, J. B., Wohlers, T. M., Fridovich-Keil, J. L., and Holden, H. M. (2000) Crystallographic evidence for Tyr 157 functioning as the active site base in human UDP-galactose 4-epimerase. *Biochemistry 39*, 5691−5701.
(49) Mulichak, A. M., Theisen, M. J., Essigmann, B., Benning, C., and Garavito, R. M. (1999) Crystal structure of SQD1, an enzyme involved in the biosynthesis of the plant sulfolipid headgroup donor UDP-sulfoquinovose. *Proc. Natl. Acad. Sci. U.S.A. 96*, 13097−13102.

DOI: 10.1021/bi501357c
Biochemistry 2015, 54, 807−819